



Modeling two-phase flow in a micro-model with local thermal non-equilibrium on the Darcy scale



Philipp Nuske^{a,*}, Olaf Ronneberger^b, Nikolaos K. Karadimitriou^d, Rainer Helmig^a, S. Majid Hassanizadeh^c

^a Department of Hydromechanics and Modelling of Hydrosystems, University of Stuttgart, Germany

^b Image Analysis Lab, Department of Computer Science, and BIOS Centre for Biological Signalling Studies, University of Freiburg, Germany

^c Department of Earth Sciences, Utrecht University, Netherlands

^d School of Chemical Engineering and Analytical Science, Faculty of Engineering and Physical Sciences, University of Manchester, Manchester, UK

ARTICLE INFO

Article history:

Received 17 December 2014

Received in revised form 16 April 2015

Accepted 20 April 2015

Available online 22 May 2015

Keywords:

Two-phase flow in porous media

Local thermal non-equilibrium

Image analysis

Determination of constitutive relations

Local equilibrium assumptions

Model calibration

Macro-scale non-equilibrium model

ABSTRACT

Loosening local equilibrium assumptions in two-phase flow in porous media gives rise to new, unknown variables. More specifically, when loosening the local thermal equilibrium assumption, one has to describe the heat transfer between multiple phases, present at the same mathematical point.

In this paper, we calibrate a macro-scale mathematical model which is free of local equilibrium assumptions to experimental observations. We emphasize the correct determination and upscaling of necessary input parameters from the experimental data achieved by image analysis. By choosing an appropriate scaling parameter, we are able to reproduce experimental measurements satisfactorily. This is a first step towards quantifying heat transfer in two-phase flow in porous media. Ultimately, our aim is to find the limits of the applicability of local equilibrium assumptions in two-phase flow in porous media.

© 2015 Elsevier Ltd. All rights reserved.

1. Introduction

One of the most prominent assumptions in the field of two-phase flow in porous media is the assumption of local equilibrium. Basically, this means that energy and mass transfer between phases take place instantaneously [e.g. [9]]. In this work, we provide tools and conceptual as well as numerical models which allow us to describe and study two-phase flow in porous media without making local thermal equilibrium assumptions: We build on the concepts explained in Nuske et al. [17] and apply the macro-scale model developed in that work. In this work, we focus on the transfer of micro-scale measurements to macro-scale properties and application of those quantities in macro-scale models. The tools provided in that regard are explained in detail and made available as free software. Here, we make a proof of concept in order to show that principal characteristics of the micro-scale experiment can be captured by the macro-scale local thermal non-equilibrium model applying the measured input parameters. This is an important step in studying the applicability of the local thermal equilibrium assumption in two-phase flow in porous media.

Pure scientific curiosity is, of course, known to boost general progress, but there are also a number of practical applications

which put the question of the applicability of local equilibrium assumptions on the agenda.

One effective technique for the cleanup of contaminated sites is the injection of hot steam into the subsurface [e.g. [18,7]]. This process involves temperature differences and flow velocities which are high compared with other flow processes in porous media. The correct prediction of contaminant behavior in this highly non-isothermal setting is crucial for solving environmental problems instead of creating new ones.

During in-situ combustion [19], heavy oil is partly oxidized in the reservoir in order to decrease its viscosity for mobilization, and ultimately production. If the temperatures of the individual phases are not correctly described, undesired reactions may take place. Or even worse: too much oil could be burnt instead of being produced.

After a severe nuclear accident, the core might collapse and can be treated as a porous medium [6,3]. It is of paramount importance to have a good understanding of the subsequent events in order to be able to orchestrate a fast cooling without causing any further (H₂) explosions.

At the interface between the subsurface and the atmosphere, two very different compartments share a boundary: the land surface. Here, evaporation takes place if the subsurface provides liquid water and the atmosphere can take up water vapor. However, flow velocities in the atmosphere can be very high and the exact

* Corresponding author.

E-mail address: Philipp.Nuske@iws.uni-stuttgart.de (P. Nuske).

interaction processes are not yet fully understood. Nonetheless, current models [20,15] assume local equilibrium.

What all these examples have in common is that they do not only involve temperature differences but also phase-change processes. In addition to that, there are to some extent sources present in the porous medium, which might prevent the system from reaching equilibrium.

The description of temperature effects by means of an energy balance equation is a standard approach in the modeling of miscible two-phase flow. However, to the best of our knowledge, there are only few approaches which allow to describe local thermal non-equilibrium in two-phase flow in porous media on the macro-scale and resolve phase-specific temperatures. Fichot et al. [6] describe local thermal non-equilibrium for the case of nuclear debris cooling, i.e. with a strong heat source present in the porous medium. However, they have to solve micro-scale closure problems in order to close the system.

Crone et al. [5] describe local thermal non-equilibrium, but only between the fluid phases and the solid phase. In other words: the fluid phases are still assumed to have locally the same temperature.

The macro-scale balance equations used in this work build on Ahrenholz et al. [2], extended in Nuske et al. [17]. In that work, local chemical and thermal non-equilibrium are allowed between the fluid phases and the solid and fluid phases respectively. To keep this work concise, we outline the main characteristics of that model briefly.

The main consequence of allowing different potentials in different phases is an increased number of primary variables. In the case of mass balance, not assuming local equilibrium leads to mole fractions in different phases not being connected via equilibrium relations. Therefore, individual balance equations are needed for each component in each phase. In the case of a two-phase two-component system, the number of mass balance equations is increased from two to four and mass transfer (i.e. the equilibration process) between the phases needs to be described. In this work, we focus on modeling experimental observations and refer to Appendix A and the literature for a discussion of the mathematical model.

In terms of energy balance, not assuming local thermal equilibrium leads to different temperatures present in the same control volume. Thus, individual energy balance equations for the respective (liquid as well as solid) phases need to be formulated. In the case of two-phase flow, the number of energy balance equations is increased from one to three and energy transfer (i.e. the equilibration process) between all phases needs to be captured. The exact structure of these balance equations is not the focus of this work. As mentioned above, the detailed discussion of the mathematical model is beyond the scope of this work. For the sake of brevity, we therefore refer to Appendix A and the literature.

In this work, we want to study the influence of heat transfer on reproducing experimental observations. The energy transfer processes between the phases are approximated by standard engineering approaches. However, no transfer relations for the case of two-phase flow in porous media could be found in the literature. Therefore, a scaling parameter, f_e , was introduced. It basically scales the heat and mass transfer relations between the respective phases, with $f_e = 0$ standing for an immiscible system and $f_e \rightarrow \infty$ representing the standard equilibrium case. A parameter study was conducted and it was found that variations in f_e lead to the expected and physically reasonable results. In this work, the macro-scale balance equations explained in Nuske et al. [17] are employed in order to simulate the experiment described in Karadimitriou et al. [11].

Karadimitriou et al. [11] presented an experimental setup for the measurement of phase specific temperatures, as well as phase

distribution, during invasion and equilibration processes in a transparent micro-model, made of Polydimethylsiloxane (PDMS). The described setup is a continued development of a mature measurement setup engineered at Utrecht University, Netherlands. In that setup, a residing wetting phase (Fluorinert) was displaced by a hot, invading, non-wetting phase (water). Both phases were liquid. This invasion took place in a quasi two-dimensional micro-model, which allowed optical as well as infrared observation. The complete experimental procedure as well as relevant information about the production process were explained in detail. Subsequently, measurement and image processing techniques were demonstrated. Finally, qualitative results and findings showcasing the usability and versatility of the platform were presented.

In this paper, we build on the modeling and experimental foundation outlined above and take one further step towards the quantitative understanding and parameter estimation in the area of local thermal non-equilibrium in two-phase flow in porous media. To be more precise, we obtain an estimate of the proposed heat transfer scaling factor f_e by means of parameter calibration. In order to accomplish this, we simulate two experimental runs of the experiment explained in Karadimitriou et al. [11] with the macro-scale local thermal non-equilibrium model explained in Nuske et al. [17] and given for completeness in Appendices A and B. By comparing simulation and experiment, we obtain a first-order approximation of the up-to-now unknown scaling parameter f_e which was suggested in Nuske et al. [17]. However, it has to be clearly stated that the goal of this work is not the exact reproduction of all presented aspects of the experimental observations. We want to give a proof of concept, demonstrating that certain features of the phase-specific temperature measurements can be reproduced by a macro-scale model employing phase-specific energy balance equations.

Solving the system on the macro scale demands the determination of a number of non-standard relations. Most prominently, this is the interfacial area between the respective phases. Therefore, the micro-scale identification and measurement of volume specific interfacial area as well as its transfer to macro-scale relations is a special focus of this work. The employed image analysis pipeline is explained in detail and provided, along with the simulation source code, under a free license.

The structure of this work is the following: In Section 2, input parameters needed for the macro-scale model are presented. Fluid and material parameters are straight forward to obtain. However, matrix properties and two-phase properties require some more effort (Section 2.2). The determination of interfacial areas, which are inevitable input parameters to the macro-scale model, require the development of a new image analysis algorithm, explained in Section 3. Building on that information, macro-scale constitutive relations are fit to the obtained data in Section 4. Modeling choices and simulation setup are explained in Section 5. Employing these input parameters, the simulations of different experimental runs are presented in Section 6. We conclude in Section 7 and deduce future research goals.

2. Input parameters

A model can only be as good as its input. Therefore, the simulation of complex systems, like two-phase flow in porous media, requires the detailed understanding of the parameters which are input to the model.

This is even more so for a non-standard model, such as the local thermal non-equilibrium model employed here. In this case, in addition to the fluid (Section 2.1) and matrix (Section 2.2) properties (and their interaction), the interfacial area available to heat

transfer is a crucial input. The determination of all interfacial areas in a micro-model has not been accomplished so far and is therefore presented in detail in Section 3.

2.1. Material & fluid properties

In order to keep the model as simple as possible, we use constant fluid properties for Fluorinert and water, see Table 1. In that table, c , ρ , λ and μ stand for the mass specific heat capacity, density, heat conductivity and viscosity of the respective phases α . Using constant properties is mostly justified by the fluids being both liquids and the comparatively moderate temperature differences during the experiment.

Although PDMS is in principle elastic, it will be modeled as a rigid, non-deforming [10] solid phase with the properties given in Table 2.

2.2. Micro-model properties

In order to measure intrinsic permeability (K), steady state flow measurements are conducted with the model and setup described in Karadimitriou et al. [10]. The flow network is completely filled with the wetting phase (Fluorinert) and one reservoir is connected to a syringe pump. Upon reaching steady state, the pressure drop along the micro-model is recorded. With all remaining quantities known, intrinsic permeability can be calculated by using Darcy’s law. The procedure is repeated several times and an error of 2%

Table 1
Fluid properties.

	c_α (kJ/kg K)	ρ_α (kg/m ³)	λ_α (W/m K)	μ_α (Pa s)
Fluorinert ^a	1.1	1860	0.065	$4.7 \cdot 10^{-3}$
Water	4.2	1000	0.6	$1 \cdot 10^{-3}$

^a 3 M [1].

Table 2
Material properties of the solid phase (PDMS, [12]).

c_s (kJ/kg K)	ρ_s (kg/m ³)	λ_s (W/m K)
1.2	970	0.15

Table 3
Intrinsic properties of the micro-model.

K (m ²)	ϕ (–)
$2.3 \cdot 10^{-10}$	0.58

of the intrinsic permeability measurements is calculated, see Table 3.

The capillary pressure – saturation curve is obtained from pressure controlled quasi-static measurements. Initially, the micro-model is fully saturated with the wetting phase. The non-wetting phase is introduced through sequential equilibrium pressure steps. For each step, an optical image of the distribution of fluids in the network is taken and the corresponding pressure difference between the reservoirs is recorded. Phase saturations are obtained by image processing. The equilibrium data points as well as a fit [21] function are shown in Fig. 4.

The porosity (ϕ) of the micro-model is also determined by image processing (Table 3). An image of the micro-model, fully saturated with the wetting phase, is used for this purpose. The measured value (58%) is close to the value expected from the design (60.5%).

3. Image analysis

We developed image analysis algorithms to extract saturation and interfacial areas from recorded images. In order to apply a consistent set of constitutive relations, the same set of images, recorded for the capillary pressure – saturation measurements (see Section 2.2), is used.

The framework first maps each recorded image to a model image of the theoretical network. Then, it uses a threshold segmentation and basic morphological operations to compute the area of the wetting and the non-wetting phases in the image, as well as the border lengths between all areas. Using the scale of the model image, the areas and lengths in pixel coordinates are scaled to real-world units. In the final step, these areas and lines are multiplied with the depth of the micro-channels to obtain an estimate of the real volumes and the interfacial areas. The detailed image analysis pipeline is described in the following sections.

3.1. Thin plate spline warping

The camera optics introduce some distortions to the image. To compensate for these distortions, and to bring each image to a standard coordinate system, we compute a mapping (warping) of the recorded image to the model image. This is done based on a set of manually defined landmark correspondences in the recorded image. The recorded gray scale image is denoted as $I : \mathbb{R}^2 \rightarrow \mathbb{R}; \mathbf{x} \mapsto I(\mathbf{x})$, see Fig. 1, right. We choose a rendered model of the micro-channel layout as reference image, see Fig. 1, left.

In this rendered model, the mask selecting the void space is given by $M_v : \mathbb{R}^2 \rightarrow \{0, 1\}$.

$$M_v(x) = \begin{cases} 1, & \text{if } x \text{ is in the void space,} \\ 0, & \text{elsewhere.} \end{cases} \tag{1}$$

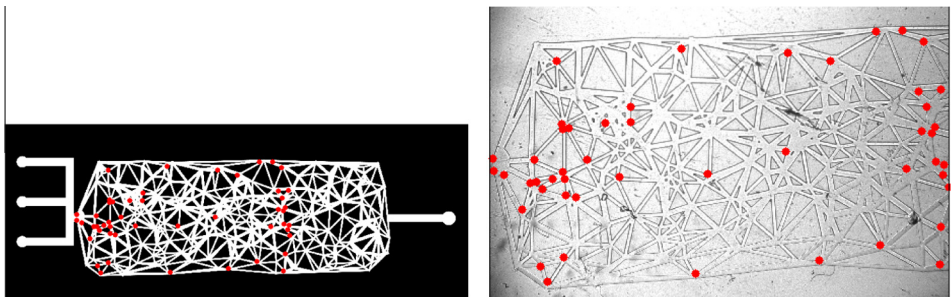


Fig. 1. Left: Selected landmarks (red dots) in the model. Right: Identified landmarks in the recorded image. (For interpretation of the references to color in this figure legend, the reader is referred to the web version of this article.)

This is also known as the characteristic function of the void space and is depicted in Fig. 1 (left) with the solid phase in black and void space in white. The landmark positions in the recorded image are denoted by $\mathbf{a}_i \in \mathbb{R}^2$, $i \in \{1, \dots, N\}$. The corresponding landmarks in the reference image are denoted as $\mathbf{b}_i \in \mathbb{R}^2$, $i \in \{1, \dots, N\}$. We compute a dense warping function $\mathbf{T}: \mathbb{R}^2 \rightarrow \mathbb{R}^2$ using thin plate spline interpolation between these landmarks [4], such that

$$\mathbf{a}_i = \mathbf{T}(\mathbf{b}_i) \quad \forall i \in \{1, \dots, N\}. \quad (2)$$

This transformation is applied to the recorded image (I) to obtain the warped recorded image (I')

$$I'(\mathbf{x}) := I(\mathbf{T}(\mathbf{x})). \quad (3)$$

We added additional landmark pairs, until all micro-channel borders in the warped image were aligned to the borders of the model image.

3.2. Segmentation

To segment the warped recorded image into the different phases, we first apply a shading correction to compensate the inhomogeneous illumination and sensitivity of the optical system. The local attenuation function $g_a: \mathbb{R}^2 \rightarrow \mathbb{R}$ is estimated from the recorded intensities of the solid phase by a GAUSSIAN weighted averaging over the solid-phase-pixels in the local surrounding

$$g_a = \frac{(M_s \cdot I') * G_\sigma}{M_s * G_\sigma}, \quad (4)$$

where $G_\sigma(\mathbf{x}) = \frac{1}{\sqrt{2\pi}\sigma} \exp\left(-\frac{x^2}{2\sigma^2}\right)$ is the GAUSSIAN smoothing kernel (here $\sigma \approx 2.2$ mm), M_s is the mask selecting the solid phase pixels, and $*$ denotes a convolution. This mask is derived from M_v by inversion and morphological erosion to exclude the micro-channel borders by

$$M_s = (1 - M_v) \ominus C_r, \quad (5)$$

where $C_r \subset \mathbb{R}^2$ describes a disk-shaped structuring element with radius r , i.e. $C_r = \{\mathbf{x} \in \mathbb{R}^2 \mid \|\mathbf{x}\| < r\}$. Here, we use an $r \approx 110$ μm . The symbol \ominus denotes the morphological erosion, which is defined for a continuous function $f: \mathbb{R}^2 \rightarrow \mathbb{R}$ with a structuring element $S \subset \mathbb{R}^2$ as

$$(f \ominus S)(\mathbf{x}) = \min_{\mathbf{k} \in S} (f(\mathbf{x} + \mathbf{k})). \quad (6)$$

The estimated attenuation function g_a is then used to compensate for all attenuation effects in the image in order to perform the subsequent threshold segmentation. The pixels belonging to the non-wetting phase are found by

$$M_n = \left[\frac{I' * G_\sigma}{g_a} < 0.5 \right] \cdot M_v, \quad (7)$$

where G_σ is a small GAUSSIAN smoothing kernel with $\sigma \approx 11$ μm to avoid noisy borders in the obtained mask. Very small regions (< 10 pixels ≈ 4800 μm^2) are eliminated from this mask using a connected component analysis. The segmentation mask for the wetting phase is then found by

$$M_w = (1 - M_n) \cdot M_v. \quad (8)$$

The respective masks are graphically shown in Fig. 2 for one equilibrium pressure step.

3.3. Estimation of macro-scale quantities

We use the obtained segmentation masks M_w and M_n from each recorded frame to estimate the volume of the wetting and the non-wetting phase as well as the interfacial areas between them and the solid phase. The analysis of an empty image (containing only the wetting phase) at the beginning of the sequence is used to define a mask of erroneously assigned pixels, originating from scratches and dust particles on the sample. These pixels are excluded from further analyses.

The volume of the wetting and the non-wetting phases is computed from the area of the corresponding segmentation mask and the constant depth d of the channels as

$$V_w = d \int_{\mathbb{R}^2} M_w(\mathbf{x}) d\mathbf{x} \quad (9a)$$

$$V_n = d \int_{\mathbb{R}^2} M_n(\mathbf{x}) d\mathbf{x}. \quad (9b)$$

From this, the calculation of wetting phase saturation is straight forward:

$$S_w = \frac{V_w}{V_w + V_n}. \quad (10)$$

The interfacial areas appear as interface border lines in the 2d image. To measure the length of these borders, they were computed as lines with single pixel width using morphological operations on the segmentation masks (here all M denote the discretized masks). b_{wn} , b_{ws} and b_{ns} stand for the wetting – non-wetting, wetting – solid and non-wetting – solid border lines

$$b_{wn} = (M_w \oplus \mathcal{N}) \cdot M_n \quad (11a)$$

$$b_{ws} = (M_w \oplus \mathcal{N}) \cdot (1 - M_v) \quad (11b)$$

$$b_{ns} = (M_n \oplus \mathcal{N}) \cdot (1 - M_v) \quad (11c)$$

with $\mathcal{N} = \left\{ \begin{pmatrix} -1 \\ 0 \end{pmatrix}, \begin{pmatrix} 1 \\ 0 \end{pmatrix}, \begin{pmatrix} 0 \\ 0 \end{pmatrix}, \begin{pmatrix} 0 \\ -1 \end{pmatrix}, \begin{pmatrix} 0 \\ 1 \end{pmatrix} \right\}$ describing the 4-neighborhood of a pixel, and \oplus denoting morphological dilation, which is defined correspondingly to the erosion (Eq. 6) as

$$(f \oplus S)(\mathbf{x}) = \max_{\mathbf{k} \in S} (f(\mathbf{x} + \mathbf{k})). \quad (12)$$

The calculated borderlines are shown in Fig. 3.

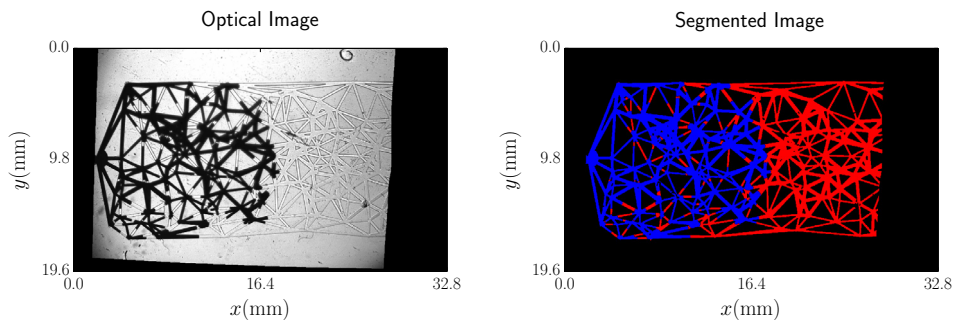


Fig. 2. Left: Optical image of a quasi-static measurement point. Right: Segmented image, M_n is depicted in blue and M_w is depicted in red. (For interpretation of the references to color in this figure legend, the reader is referred to the web version of this article.)

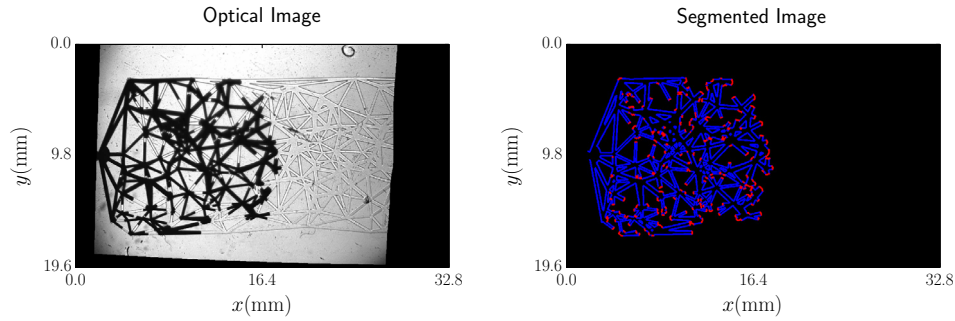


Fig. 3. Left: Optical image of a quasi-static measurement point. Right: Segmented image, b_{ns} is depicted in blue and b_{wn} is depicted in red. Both borderlines are grown for visualization. (For interpretation of the references to color in this figure legend, the reader is referred to the web version of this article.)

To estimate the true length of the resulting lines, the centers between two adjacent pixels are connected to an open polygon. End pixels, corner pixels (at corners with an angle of 90° or more) and center pixels at line junctions are also added to that polygon. The measured length of such a polygon differs in the worst case approximately 3% from the true length of a straight line, which we consider precise enough for further evaluations.

The actual quantities of interest in this context are the volume specific interfacial areas between the wetting and non-wetting as well as non-wetting and solid phases, a_{wn} and a_{ns} , as they represent the cross-sectional area available to heat transfer. The remaining interfacial area between the wetting and the solid phase (a_{ws}) is the difference of the total solid surface, a_s , and a_{ns} . By means of the given measurements, they are actually straight forward to compute from Eqs. (11). The respective lengths of the border lines need to be multiplied by the micro-model depth d and divided by the observed volume of the micro-model (V_{mm})

$$a_{wn} = \frac{db_{wn}}{V_{mm}} \quad (13a)$$

$$a_{ns} = \frac{db_{ns}}{V_{mm}} \quad (13b)$$

3.4. Implementation details & code availability

The image analysis pipeline is implemented in Matlab R2013a. The recorded images have a pixel size of $11 \mu\text{m}$, the model image was rendered with a pixel size of $21.9 \mu\text{m}$. The image analysis source code (along with the raw images) and the flow simulation source code is provided to the scientific community under the GNU General Public License [GPLv2, [8]]. It can be accessed as a DuMu^x module only depending on the stable release of DuMu^x (dumux-pub/Nuske-2014a). Please refer to the online documentation of DuMu^x¹ for technical details.

4. Constitutive relations

Building on the data obtained by means of the image analysis procedure, we briefly present the fit constitutive relations. These constitutive relations are required in the non-equilibrium macro-scale model and are therefore crucial to this work.

Capillary pressures are identified as the difference between the pressures on the boundaries of the flow network during quasi-static measurements. Wetting phase saturations, volume specific wetting – non-wetting and non-wetting – solid interfacial areas have been obtained in Section 3.

From these values, a van Genuchten [21]-type curve was fit to the measured $p_c - S_w$ data points and is shown in Fig. 4. Relative

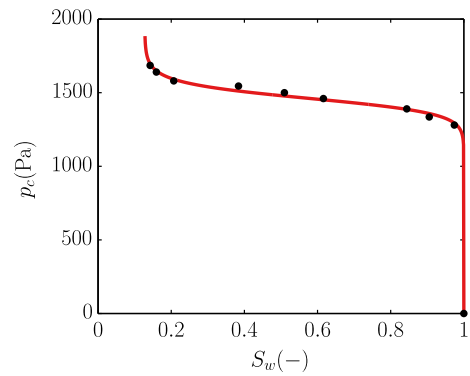


Fig. 4. Measured data points with fit VAN GENUCHTEN function. The fit coefficients are given in Table 4.

Table 4

VAN GENUCHTEN parameters of the capillary pressure – saturation fit (index p_c) and relative permeability – saturation fit (index k_r). For each fit, the coefficient of determination R^2 is given.

α_{p_c} (1/Pa)	n_{p_c} (-)	S_{wr}	$R_{p_c}^2$	m_{k_r}	$R_{k_r}^2$
$6.8 \cdot 10^{-4}$	28.2	0.13	0.99	1.70	0.92

permeabilities are obtained from independent measurements of the non-wetting phase relative permeability. A van Genuchten [21]-type (in conjunction with Mualem [16]) relative permeability curve is fit to the data points and the obtained fitting coefficient is transferred to the wetting phase relative permeability, see Table 4.

Linear relations (Eqs. (14a) and (14b)) are fit to the volume specific interfacial area data, see Fig. 5 and Table 5. The remaining interfacial area (a_{ws}) is obtained as the difference of total solid surface a_s and a_{ns} .

$$a_{wn} = a_1 S_w - a_1 \quad (14a)$$

$$a_{ns} = a_2 S_w - a_2 \quad (14b)$$

$$a_{ws} = a_s - a_{ns} \quad (14c)$$

All fits were conducted by means of a non-linear least squares fitting tool [13]. The image analysis procedure outlined above was conducted on the same data set as used for the capillary pressure relation. However, in order to reduce the influence of the boundary, the last two images are excluded, as some of the interfacial area had already left the field of view of the camera.

Naturally, the interfacial area between the wetting and non-wetting phases needs to be zero for saturations of one and zero, respectively. However, the presented equations fit the

¹ <http://www.dumux.org>

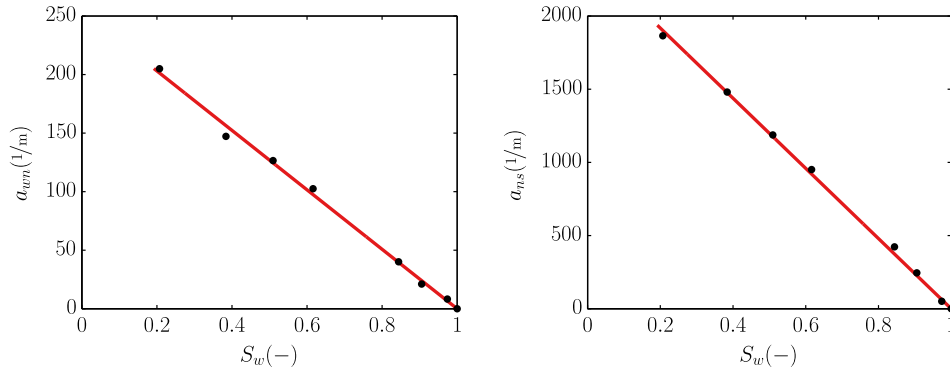


Fig. 5. Measured data points with fit functions for $a_{wm} - S_w$ (left) and $a_{ns} - S_w$ (right) relations, see Eq. (14a) and (14b) and Table 5. Both relations are a unique function of S_w because only data of a primary drainage process is fit.

Table 5

Fit parameters and coefficients of determination, see Eqs. (14a) and (14b) and Fig. 5. For each fit, the coefficient of determination R^2 is given.

a_1	R_1^2	a_2	R_2^2
-253.85	0.99	-2397	0.99

obtained data very well, especially for partially water saturated porous media. In order to capture the full scale of possible saturations, more measurements are necessary and extended parametrizations are needed. However, we stick to the simplest possible description of the available data.

More research is also needed with respect to the role of residual saturations and the associated interfacial areas during energy exchange processes. For the time being, we stick to the presented equation.

5. Experimental & modeling setup

The experimental setup has been exhaustively described in Karadimitriou et al. [11]. Here, we will focus on the modeling decisions, made in order to simulate the experiment and ultimately calibrate heat transfer coefficients. The most basic decision is how to represent the physical setup which is to be simulated. We chose a one-dimensional model, as the process of interest has a dominant direction. The flow processes in the micro-model are represented by a macro-scale description: There is no detailed information about geometry, but the properties of the medium and the interaction with the fluid phases are represented on a volume-averaged basis.

5.1. Balance equations

We employ the same balance equations as explained in Nuske et al. [17] and briefly presented in Appendices A and B. The point of most importance is that Nuske et al. [17] suggest a heat transfer relation between phases which involves a parameter, f_e . This parameter scales a standard heat transfer relation in order to capture heat transfer in the scope of two-phase flow in porous media. Here, we will try and estimate this parameter by comparing simulation results and experimental observations.

In the example presented in Nuske et al. [17], temperature differences arose from evaporation processes. Here, temperature differences are externally applied. Therefore, we choose to select a model which is as simple as possible. Solubility effects can be neglected, as the chosen phases are virtually immiscible. Technically, this is implemented by setting the equilibrium, initial and injected mole fractions (x_{α}^{κ}) to zero and unity, respectively, which results in pure phases. As the micro-model was placed horizontally during all experiments, gravitational effects do not play an important role and are neglected.

In terms of numerical implementation, a vertex centered finite volume discretization is used. Time discretization is accomplished fully implicitly. All equations are assembled in a fully coupled manner in one non-linear system of equations for the new time-level. The system is solved by means of the NEWTON method. All balance equations, constitutive relations and the thermodynamical framework are part of DuMu^x and are freely available, see Section 3.4 for details.

In this work, the index w stands for the *wetting* phase. With the solid phase being made of silanized PDMS [11], the wetting phase is *not* water but Fluorinert.

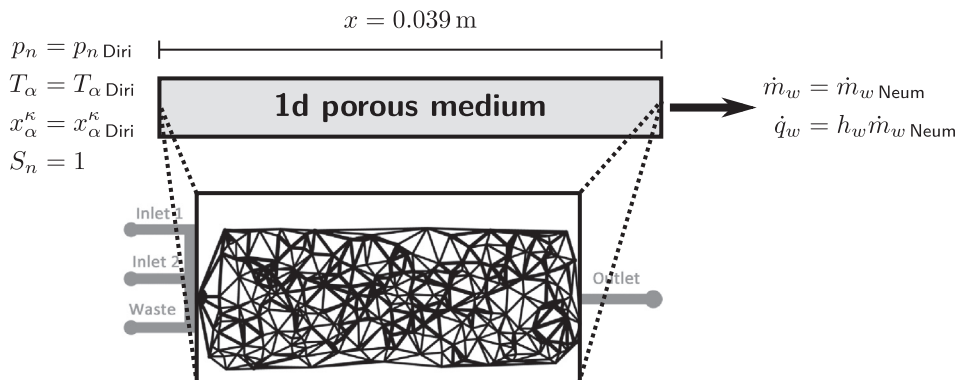


Fig. 6. Boundary conditions as well as model abstraction of the simulation.

5.2. Initial and boundary conditions

Fig. 6 shows the one-dimensional modeling concept as well as the chosen boundary conditions. Due to the high circulation flow rate [11] constant conditions are assumed at the inflow to the micro-model. Therefore, DIRICHLET values are set at the left-hand side of the modeling domain. On the right-hand side, NEUMANN values (\dot{m}_{Neum}) capture the withdrawal rates of fluid from the micro-model. Initial conditions are given in Table 6.

In this work, two experimental runs, mainly differing in the withdrawal rates imposed on the right-hand side, will be studied. The two experimental runs will be termed *low-rate* and *high-rate*, see Table 6 for the respective values.

5.3. Implementation of heat loss

As the micro-model is not placed in a complete vacuum, it exchanges energy with its surrounding. However, the topic of this

work is the study and simulation of flow processes in porous media. Therefore, the exchange processes between micro-model and surrounding are not explicitly included but captured via boundary conditions.

We conceptualize the micro-model as a flat plate and use literature [14] correlations for heat transfer coefficients (h_c) from a hot plate. Two contributions are assigned, heat loss from the top and from the bottom of a hot plate. At each vertex, with associated surface A , these losses occur according to

$$\dot{Q}_{\text{top}} = h_{c\text{top}} A (T_{\text{amb}} - T_s) \quad (15)$$

$$\dot{Q}_{\text{bottom}} = h_{c\text{bottom}} A (T_{\text{amb}} - T_s), \quad (16)$$

with the constant ambient temperature T_{amb} , chosen to be identical to the initial temperature. The heat losses are attributed exclusively to the solid phase because the outside of the micro-model consists of PDMS. Radiation losses are neglected due to low temperatures.

6. Simulation & experiment

The goal of this work is to gain a better understanding about the heat transfer between phases in two-phase flow in porous media processes. To be more precise, we want to estimate the unknown scaling parameter f_e , see [17] or Appendix B.

In order to accomplish this, two experimental runs (*low-rate* and *high-rate*) are analyzed. They are simulated as explained

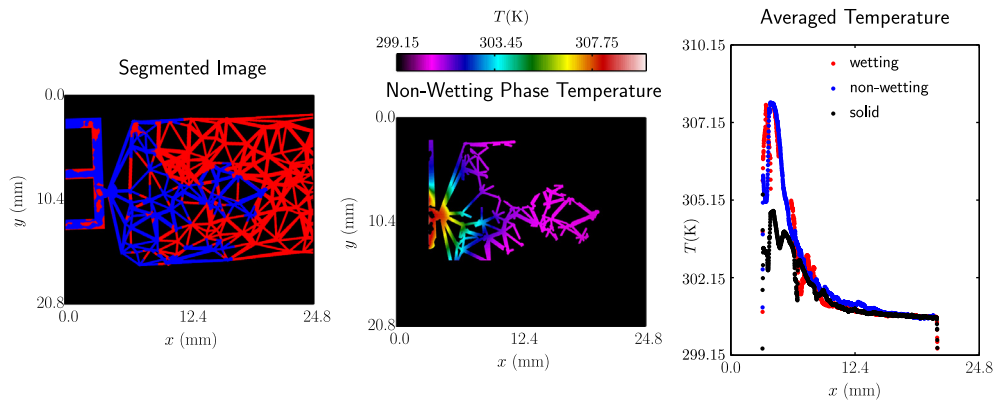


Fig. 7. Left: The mask selecting the invading non-wetting phase is depicted in blue. Middle: The part of the infrared measurement attributed to the non-wetting phase. Right: Averages in y -direction of the respective phase temperatures, see movie [NuskeEtAlThermalNonEquil_1.avi](#). (For interpretation of the references to color in this figure legend, the reader is referred to the web version of this article.)

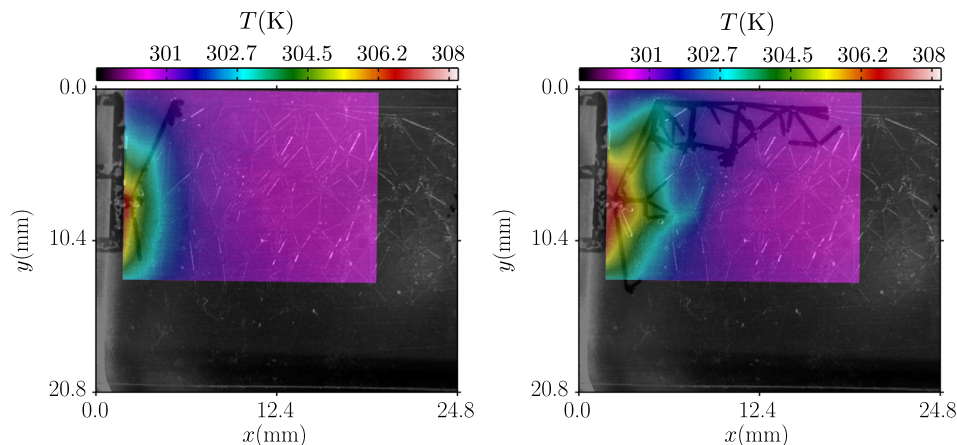


Fig. 8. Overlay of *low-rate* temperature information and optical image after 10 s (left) and 40 s (right), see movie [NuskeEtAlThermalNonEquil_2.avi](#) (showing a longer period).

above with a varying f_e and the unknown scaling parameter f_e is selected by comparing simulation and experiment.

6.1. Line averaging of temperature

For comparing the measurements and the simulations, the information obtained during the simultaneous optical and thermal imaging experiment needs to be condensed. We choose to average the temperature information in y -direction. In other words: each point in x -direction, observed by the infrared camera, is assigned y -direction-averaged temperatures. In order to assign the temperature information to the respective phases, only those points where a phase resides are included in the average. This information is obtained by means of the image analysis procedure described in Karadimitriou et al. [11].

The procedure for obtaining the one dimensional line averages of T_w , T_n and T_s is shown in Fig. 7. This condensed information is compared with simulation results in the next section.

6.2. Matching simulation results to experimental observations

First, we present the low-rate experiment and simulation. Fig. 8 shows the micro-model experiment after 10 s and 40 s with temperature information superimposed.

Fig. 9 shows the line averages of temperatures, explained above. In this figure, the beginning of the line average is moved to the

left-hand side of the flow-network and the right-hand side of the plot is dictated by the right-hand side of the field of view of the infrared camera.

Figs. 10–13 show simulations of the low-rate experiment. The heat transfer scaling parameter f_e takes values of 0.1, 0.5, 1 and 10. The scale of the plot is chosen such that the whole modeling domain is depicted.

The temperature difference at the inflow after 10 s is matched best in Fig. 10. However, at both observed times, the temperature of the solid phase is not the lowest temperature, as it is observed in the experiment, see Fig. 9. Figs. 12 and 13 both show too small a temperature difference in the inflow region when comparing to the experiment.

We therefore conclude that simulating the experiment with a scaling coefficient of $f_e = 0.5$ matches the low-rate experiment best. However, two important experimental observations cannot be matched. First, in the experiment, wetting and non-wetting temperature are close with the solid temperature being below. In the simulation, solid and wetting temperature are close with the non-wetting temperature above. Of course, this can be explained by the interfacial area between wetting and solid phase (a_{ws}) being an order of magnitude bigger than the interfacial area between non-wetting and wetting phase (a_{wn}). However, this is a notable discrepancy between simulation and experiment.

Furthermore, the front velocity in the simulation is faster than in the experiment and the locations of the invasion fronts of

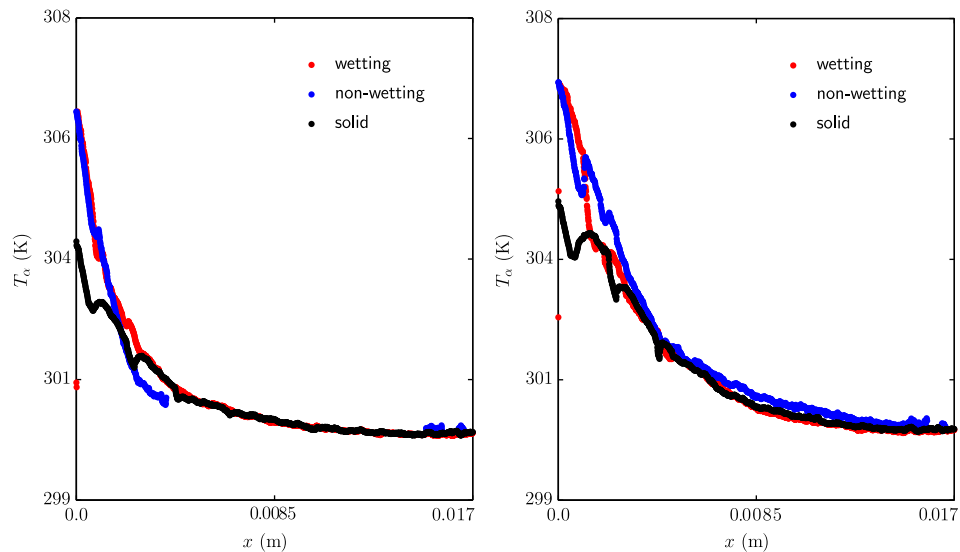


Fig. 9. Experimental measurements, low-rate. Left: 10 s after start of invasion, Right: 40 s after start of invasion, see movie [NuskeEtAlThermalNonEquil_3.avi](#).

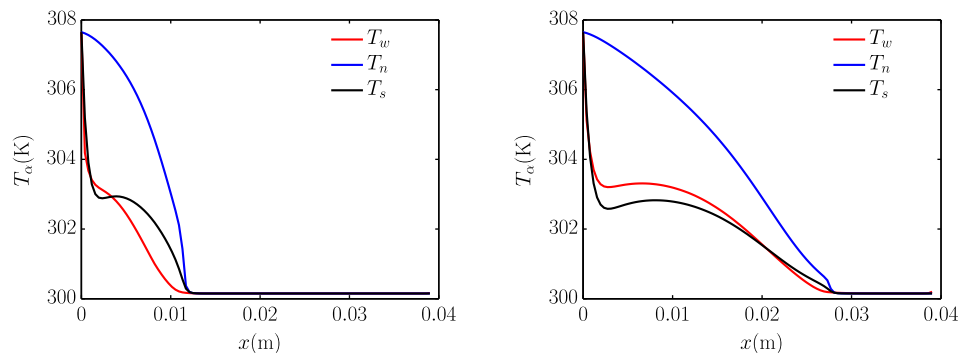


Fig. 10. Simulation of the experiment, low-rate. Left: 10 s after start of invasion, Right: 40 s after start of invasion, $f_e = 0.1$.

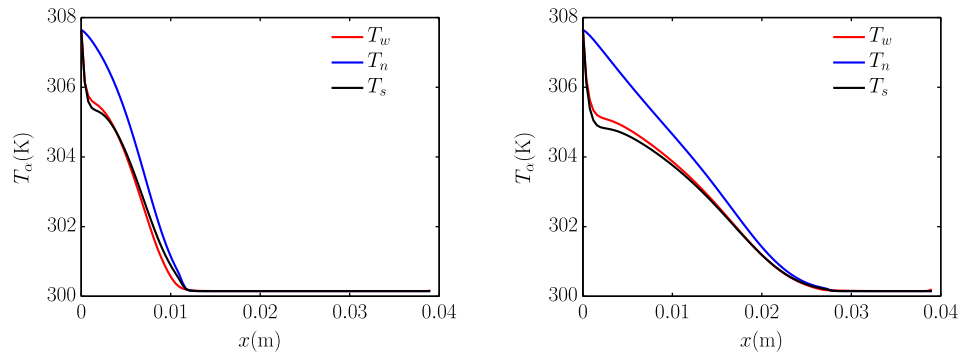


Fig. 11. Simulation of the experiment, low-rate. **Left:** 10 s after start of invasion, **Right:** 40 s after start of invasion, $f_e = 0.5$.

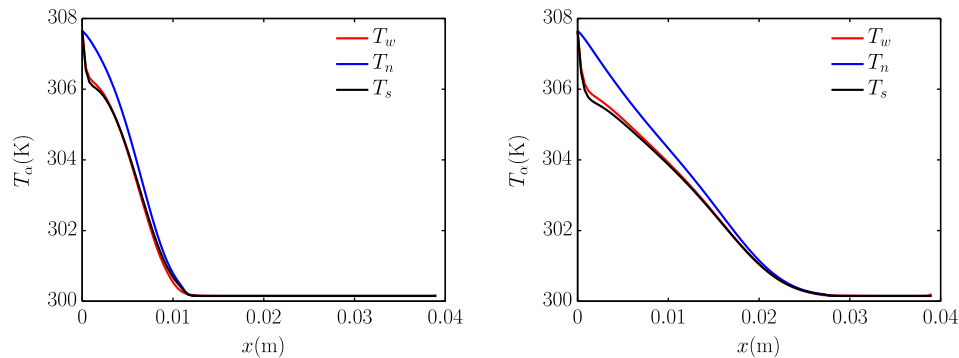


Fig. 12. Simulation of the experiment, low-rate. **Left:** 10 s after start of invasion, **Right:** 40 s after start of invasion, $f_e = 1$.

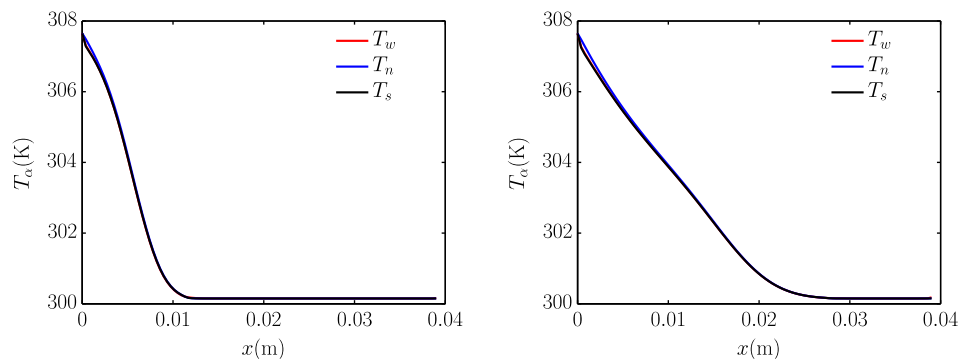


Fig. 13. Simulation of the experiment, low-rate. **Left:** 10 s after start of invasion, **Right:** 40 s after start of invasion, $f_e = 10$.

simulation and experiment could not be matched. We therefore chose to plot simulation and experimental results on their native rather than the same scale. In Section 6.3 an explanation for this observation is given.

After having presented the matching of the low-rate experiment with simulation results, we now present experimental observations and simulations of the high-rate experiment.

Fig. 14 gives an impression of the high-rate experiment after 5 s and 10 s and Fig. 15 gives the line averages of the observed temperatures.

Figs. 16–19 show simulations of the high-rate experiment with heat transfer scaling factors f_e of 0.1, 0.5, 1 and 10, respectively.

Basically, the same reasoning as given for the low-rate experiment and simulation hold. This is in itself encouraging: The model behavior is consistent and behaves as expected with respect to a

change in boundary conditions. We therefore conclude that for the given boundary conditions and variations of parameters, a heat transfer scaling factor of $f_e = 0.5$ is the best choice.

However, it has to be noted that the lowest $f_e = 0.1$ gives the best match for the temperature difference at the entrance. The incorrect behavior of the solid phase temperature can be attributed to too rough an approximation of the heat losses to the surrounding. Higher heat losses would decrease solid phase temperature, as observed in the experiment.

6.3. Limitations of the chosen boundary conditions

Fig. 20 shows the pressure distribution of the low-rate simulation after 2 s simulated time. As explained in Section 5, on the left boundary a DIRICHLET value of $S_w = 0$ and in the domain an initial saturation of $S_w = 0.999$ is set. In other words: two adjacent nodes

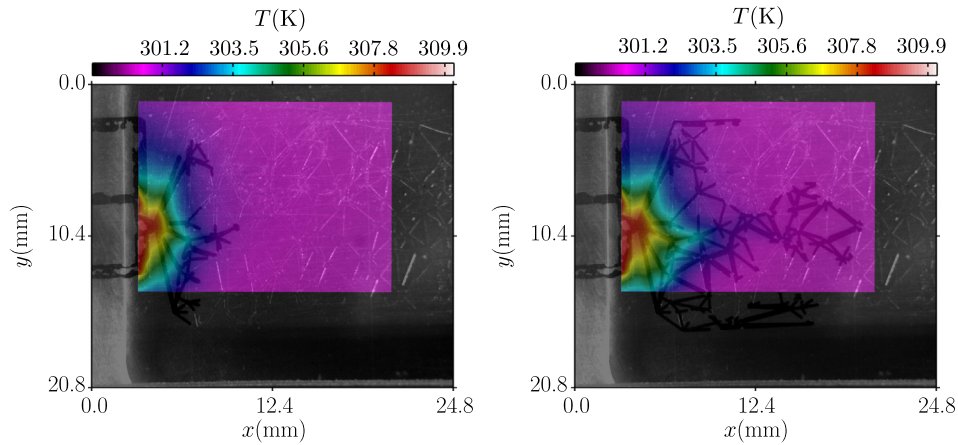


Fig. 14. Overlay of high-rate temperature information and optical image after 5 s (left) and 10 s (right), see movie [NuskeEtAlThermalNonEquil_4.avi](#) (showing a longer period).

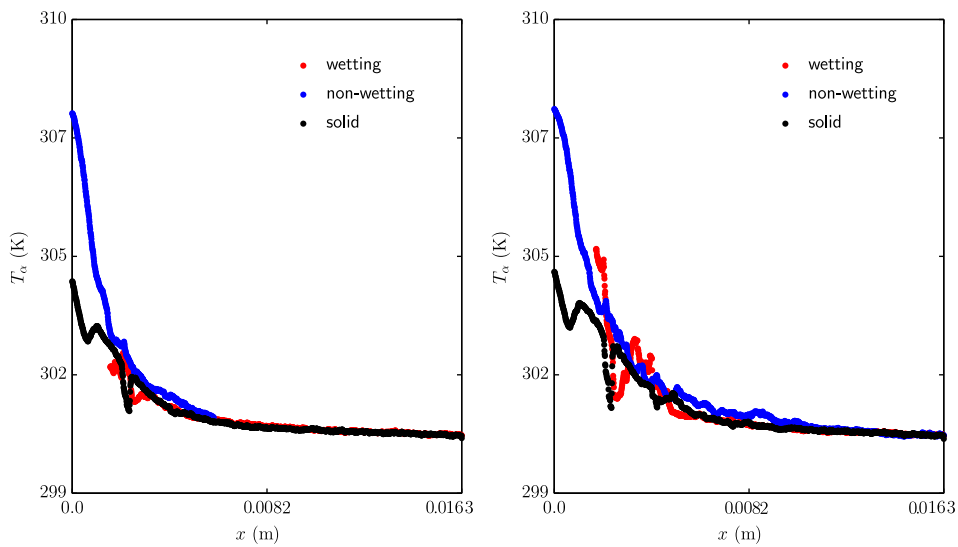


Fig. 15. Experimental measurements, high-rate. Left: 5 s after start of invasion, Right: 10 s after start of invasion, see movie [NuskeEtAlThermalNonEquil_5.avi](#).

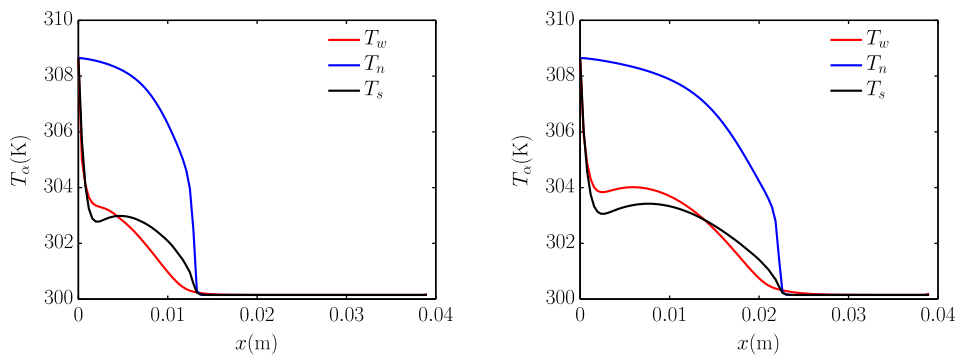


Fig. 16. Simulation of the experiment, high-rate. Left: 5 s after start of invasion, Right: 10 s after start of invasion, $f_e = 0.1$.

have states corresponding to the very ends of the capillary pressure – saturation curve (Fig. 4). This leads to a big gradient in capillary pressure and thus in the wetting phase pressure. This gradient causes a flux of the wetting phase to leave the left-hand side of

the domain. This happens regardless of the zero mobility of the wetting phase on the left-hand boundary: Mobilities are either upwinded or obtained by central spatial weighting. This way, the non-zero upstream mobility is transferred to the boundary node.

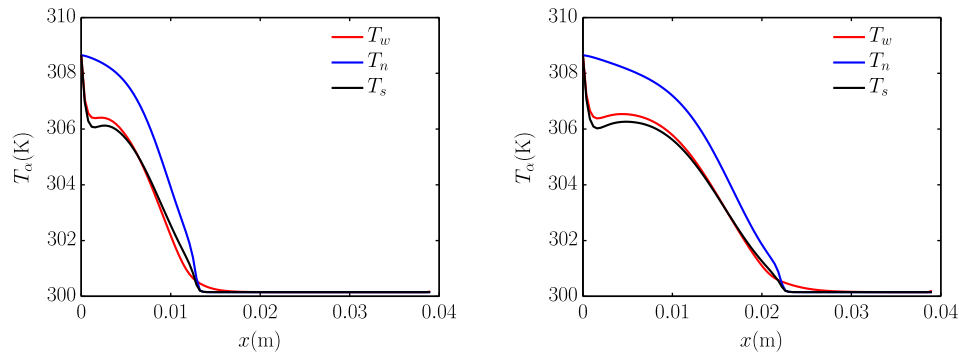


Fig. 17. Simulation of the experiment, high-rate. **Left:** 5 s after start of invasion, **Right:** 10 s after start of invasion, $f_e = 0.5$.

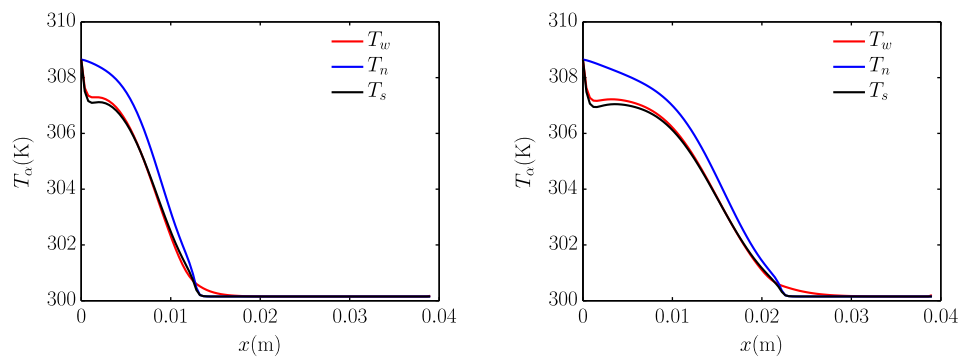


Fig. 18. Simulation of the experiment, high-rate. **Left:** 5 s after start of invasion, **Right:** 10 s after start of invasion, $f_e = 1$.

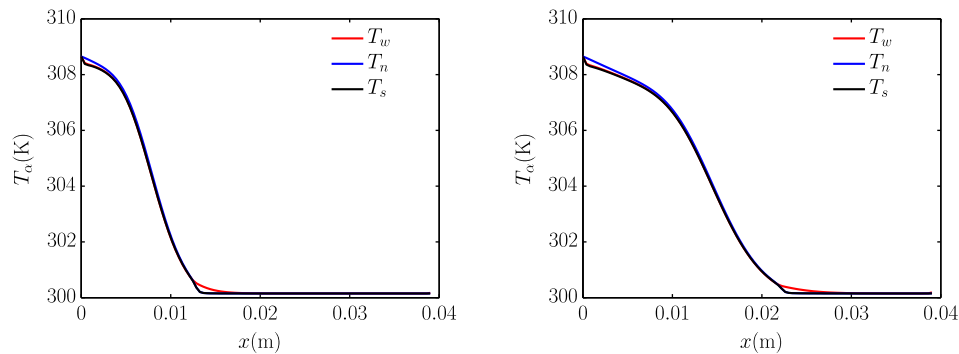


Fig. 19. Simulation of the experiment, high-rate. **Left:** 5 s after start of invasion, **Right:** 10 s after start of invasion, $f_e = 10$.

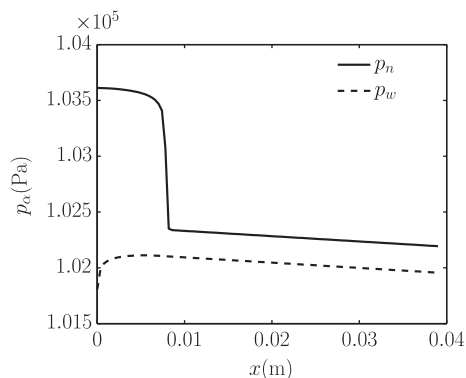


Fig. 20. Pressure distribution in the simulated experiment. Capillary pressure causes an unintended pressure gradient to the left in the wetting phase.

In order to fulfill mass conservation, more mass of the non-wetting phase has to enter the domain than caused by the NEUMANN boundary condition on the right-hand side alone.

Although this behavior fulfills the physical constraints (conservation equations, constitutive relations) formulated in the model, it leads to a behavior which is not observed in the experiment. The main result of the described effect is that too much mass of the non-wetting phase is in the system and the front locations cannot be exactly matched between simulation and experiment.

7. Summary & conclusion

In this work, the experiment described in Karadimitriou et al. [11] was successfully simulated by means of a one-dimensional macro-scale model, developed in Nuske et al. [17].

We provided detailed information about the simulation setup and employed material parameters. In order to obtain relevant input parameters to the macro-scale model, new image analysis algorithms have been developed and provided under a free license.

A number of issues remain unsolved in this context or had to be roughly approximated. First, and most notably, this is the role of heat losses to the environment. We chose an empirical formula, valid for free convection from a horizontal plate. However, the accuracy of such a formula remains open to validation in view of the given dimensions of the micro-model. The best approach would be to place the micro-model in a vacuum during the experiment in order to have good control over boundary conditions.

The role of residual saturations, and their associated interfacial areas, during kinetic energy exchange is to the best of our knowledge poorly understood. Up to now, residual interfacial areas and bulk phase interfacial areas are treated identically although residuals are not connected to bulk phases. Under the given flow conditions, they remain immobile and should therefore be treated differently from the bulk phases.

In this work, we have chosen to describe both the experiment and the simulation one-dimensionally. Given the dimensions of the system, this choice can be questioned and should be the subject of further studies. Actually, the decision to model the micro-model experiment by means of a macro-scale model needs to be better founded. Interesting tools in this regard are pore-network models, which can be seen as volume-averaging tools.

With respect to the imaging setup, the weakest points remain the synchronization of image streams [11] and the limited field of view of the infrared camera. In Section 6.3, we pointed out that the chosen boundary conditions do not perfectly match the observed behavior of the system.

In spite of the listed limitations of the presented model, the novelty and scientific contribution of the presented work are substantial. This is the first time for phase specific energy balances to be used in the simulation of an actual experiment. Furthermore, the experimental setup is new in its accessibility to optical and thermal observation. This is remarkable as it allows the phase specific attribution of temperatures. In other experimental setups in two-phase flow in porous media, it is often unclear or hard to control which temperature is actually measured. The detailed information as well as the decision to employ free and open-source software development strategies make our results open for testing and continuation.

We give an order of magnitude estimate of the alleged heat transfer scaling factor of $f_e = 0.5$ for this setup.

The ultimate goal of our work is to study the correctness and applicability of the local thermal equilibrium assumption in two-phase flow in porous media. Therefore, the reasonable reproduction of the experimental observations can be taken as the point of origin for multiple further paths of research.

First of all, it has to be clearly stated that local thermal non-equilibrium is not of major importance for the given setup and boundary conditions. Therefore, either temperature differences between phases could be increased or, more interestingly, heat sources should be introduced in one of the present phases. This can be motivated by chemical reactions taking place or by the cooling of a severely damaged nuclear reactor core.

Another interesting direction of research is the study of averaging and the choice of appropriate models. The choice of using a one-dimensional model could be questioned. Beyond this question, the applicability of macro-scale models to this type of problem could be challenged. Interesting tools in this respect are pore-network models which can be seen as tools for volume averaging.

By the provided experimental, analysis and modeling tools, we give a solid foundation for the further study of local equilibrium assumptions in two-phase flow in porous media.

Conflict of interest

None declared.

Acknowledgement

The authors would like to thank Dani Or (ETH Zurich) for providing the infrared camera used in this work. Conduction and planning of the experiment was only possible due to the experienced and deliberate work of Pieter Kleingeld (Utrecht University). The contributions of Olaf Ronneberger were supported by the Excellence Initiative of the German Federal and State Governments: BIOS Centre for Biological Signalling Studies (EXC 294). Financial support of the Ministry of Science, Research and the Arts of the State of Baden-Württemberg is gratefully acknowledged.

All simulation source code and image analysis source code, along with the original images, can be obtained as a DuMu^x module: svn+ssh://luftig/home/svn/DUMUX/dumux-pub/Nuske2014a under a free license. Please refer to www.dumux.org for details on how to obtain this information.

We would like to thank the anonymous reviewers for their helpful and timely review of the manuscript.

Appendix A. Non-equilibrium mass conservation

For completeness, we will briefly present the mathematical model for mass conservation employed in this work. For a more detailed explanation we refer to previous work [17]. The mathematical model for mass conservation is capable of describing local chemical non-equilibrium. In this context, local chemical non-equilibrium amounts to the components in the different phases of the same representative elementary volume (REV) not necessarily being connected via equilibrium relations. However, in the context of this work, immiscible flow is described. Although the presented equations are the ones used in the numerical simulation, mass transfer between phases is switched off by only allowing pure phases. However, we choose to discuss the actually implemented equations, as opposed to a simplified version.

Similar to the standard set of balance equations [9] there is a storage term, a flux term and a source term. Each of these terms has to be given for each component in each phase, leading to four balance equations for the case of a two-phase two-component system. This approach builds on the work presented in Ahrenholz et al. [2] with a refined mass exchange term and results in the following set of balance equations for a two phase, two component system:

$$\begin{aligned} \frac{\partial(\phi S_w \varrho_w x_w^w)}{\partial t} + \nabla \cdot (\varrho_w x_w^w \mathbf{v}_w + \mathbf{j}_w^w) \\ = \underbrace{q_w^w - \varrho_w f_m \text{Sh}(\text{Re}, \text{Sc}) a_{wn} \frac{D_{wn}^{w \text{pm}}}{L} (x_{n \text{equil}}^w - x_n^w)}_{-\hat{n}_{wn \rightarrow n}^w} \end{aligned} \quad (\text{A.1a})$$

$$\begin{aligned} \frac{\partial(\phi S_w \varrho_w x_w^n)}{\partial t} + \nabla \cdot (\varrho_w x_w^n \mathbf{v}_w + \mathbf{j}_w^n) \\ = \underbrace{q_w^n + \varrho_w f_m \text{Sh}(\text{Re}, \text{Sc}) a_{wn} \frac{D_{wn}^{n \text{pm}}}{L} (x_{n \text{equil}}^n - x_n^n)}_{\hat{n}_{wn \rightarrow w}^n} \end{aligned} \quad (\text{A.1b})$$

$$\frac{\partial(\phi S_n \rho_n x_n^w)}{\partial t} + \nabla \cdot (\rho_n x_n^w \mathbf{v}_n + \mathbf{j}_n^w) = \underbrace{q_n^w - \rho_n f_m \text{Sh}(\text{Re}, \text{Sc}) a_{wn} \frac{D_{wn}^w}{L} (x_{n\text{equil}}^w - x_n^w)}_{\dot{n}_{wn \rightarrow n}^w} \quad (\text{A.1c})$$

$$\frac{\partial(\phi S_n \rho_n x_n^n)}{\partial t} + \nabla \cdot (\rho_n x_n^n \mathbf{v}_n + \mathbf{j}_n^n) = \underbrace{q_n^n - \rho_n f_m \text{Sh}(\text{Re}, \text{Sc}) a_{wn} \frac{D_{wn}^n}{L} (x_{n\text{equil}}^n - x_n^n)}_{-\dot{n}_{wn \rightarrow w}^n} \quad (\text{A.1d})$$

In general, the index w stands for the wetting phase and the index n stands for the non-wetting phase. The exponents w, n stand for the main components of the respective phases.

The storage terms represent the change of a component's mass for a given point. The flux terms have two contributions: an advective (velocity \mathbf{v}) and a diffusive (diffusive flux \mathbf{j}) part. There are also two contributions to the source terms. Either from an external source (injection/reaction q) or from exchange between the phases.

As pointed out above, we only consider pure phases (mole fractions x are either unity or zero) in this work. Therefore, there is no mass exchange between phases and the respective terms in the balance equations will not be further discussed in this scope. Please refer to [17] for a discussion of the full set of balance equations including miscible phases and evaporation.

The porosity of the porous medium is ϕ and the saturation of the phases is given by S_α . ρ_α stands for the density of the respective phases. \mathbf{v}_α is a cross section specific velocity in a porous medium. In this work, we use extended Darcy's law in order to calculate velocity

$$\mathbf{v}_\alpha = -K \frac{k_{rx}}{\mu_\alpha} (\nabla p_\alpha - \rho_\alpha \mathbf{g}). \quad (\text{A.2})$$

Here, \mathbf{g} is the vector of gravity. K , k_{rx} and μ_α stand for the permeability of the porous medium, the relative permeability of phase α and the viscosity of phase α .

Appendix B. Non-equilibrium energy conservation

In this section, we will quickly present the equations used to describe local thermal non-equilibrium on the macro-scale. Individual temperatures (T_w, T_n, T_s) are allowed in all phases (wetting, non-wetting and solid phases, indices w, n, s) in the same REV. Therefore, each phase is attributed an individual energy balance. The caloric state variables internal energy (u_α) and enthalpy (h_α) are defined for each phase. The equations are given for completeness, a more detailed discussion is given in Nuske et al. [17].

The formulation of energy balance equations for the individual phases follows a straight forward train of thought: The phases do not have the same temperature. Therefore, they exchange energy which is described via a standard heat transfer ansatz. The local thermal non-equilibrium description builds on the work of Ahrenholz et al. [2].

In addition to the transport mechanisms in the case of the mass balance equations (advection and diffusion), energy can also move via conduction. A FOURIER description is used in order to describe the phase specific heat conduction with the thermal conductivity λ .

The source terms of the fluid phase energy balances have four contributions: Energy can either be introduced associated to a mass injection (q^k) or without injecting mass (q^{energy}), e.g. via heating. Each phase can exchange energy with the other two phases via two mechanism: due to different temperatures (conduction) or due to mass exchange and the associated energy transfer. The

latter will not be discussed in this work, as immiscible phases are considered.

In the energy balance equation for the solid phase the storage term captures the change of energy via the heat capacity (c_s) and the change of temperature (T_s) of the solid phase. The only flux possible in the solid phase is conduction. There are three possible source terms to the solid phase: it can either be supplied with heat from external sources or from conductive heat exchange from other phases.

The described system amounts to the following set of balance equations for three phases:

$$\begin{aligned} \frac{\partial(\phi \rho_w S_w u_w)}{\partial t} + \nabla \cdot \left(\rho_w \mathbf{v}_w h_w + \sum_K \mathbf{j}_w^K h_w^K \right) - \nabla \cdot (\phi S_w \lambda_w \nabla T_w) \\ = \underbrace{h_w^n \sum_K h_w^K q_n^K + q_w^{\text{energy}} + f_e \text{Nu}(\text{Re}, \text{Pr}) a_{wn} \frac{\bar{\lambda}_{wn}}{L} (T_n - T_w)}_{\dot{e}_{n \rightarrow w}} \\ + \underbrace{f_e \text{Nu}(\text{Re}, \text{Pr}) a_{ws} \frac{\bar{\lambda}_{ws}}{L} (T_s - T_w)}_{\dot{e}_{s \rightarrow w}} + \sum_K \dot{n}_{wn \rightarrow w}^K h_n^K \end{aligned} \quad (\text{B.1a})$$

$$\begin{aligned} \frac{\partial(\phi \rho_n S_n u_n)}{\partial t} + \nabla \cdot \left(\rho_n \mathbf{v}_n h_n + \sum_K \mathbf{j}_n^K h_n^K \right) - \nabla \cdot (\phi S_n \lambda_n \nabla T_n) \\ = \underbrace{h_n^w \sum_K h_n^K q_w^K + q_n^{\text{energy}} - f_e \text{Nu}(\text{Re}, \text{Pr}) a_{wn} \frac{\bar{\lambda}_{wn}}{L} (T_n - T_w)}_{-\dot{e}_{n \rightarrow w}} \\ + \underbrace{f_e \text{Nu}(\text{Re}, \text{Pr}) a_{ns} \frac{\bar{\lambda}_{ns}}{L} (T_s - T_n)}_{\dot{e}_{s \rightarrow n}} + \sum_K \dot{n}_{wn \rightarrow n}^K h_w^K \end{aligned} \quad (\text{B.1b})$$

$$\begin{aligned} \frac{\partial((1-\phi) \rho_s c_s T_s)}{\partial t} - \nabla \cdot ((1-\phi) \lambda_s \nabla T_s) \\ = \underbrace{q_s^{\text{energy}} - f_e \text{Nu}(\text{Re}, \text{Pr}) a_{ws} \frac{\bar{\lambda}_{ws}}{L} (T_s - T_w)}_{-\dot{e}_{s \rightarrow w}} - \underbrace{f_e \text{Nu}(\text{Re}, \text{Pr}) a_{ns} \frac{\bar{\lambda}_{ns}}{L} (T_s - T_n)}_{-\dot{e}_{s \rightarrow n}} \end{aligned} \quad (\text{B.1c})$$

The conductive heat transfer between the phases is captured by the expressions marked with underbraces. A well-known engineering approach is chosen: the heat transferred is equal to a dimensionless number times the (volume-averaged) crosssectional area (a_{wn}, a_{ws}, a_{ns}) available to the heat flux, times the averaged heat conductivity times the driving temperature difference between the respective phases divided by a characteristic length of the system, L . In detail, a_{wn} stands for the volume-averaged interfacial area between wetting and non-wetting phase, a_{ws} stands for the volume-averaged interfacial area between the wetting and solid phase and a_{ns} stands for the volume-averaged interfacial area between the non-wetting and solid phase.

[...] The dimensionless number for the case of heat transfer is the *NUSSELT* number which is a function of the flow regime – *Re* – and the fluid-specific *PRANDTL* number – *Pr*, see Table B.7. In there, c_p stands for heat capacity at constant pressure, α is the heat transfer coefficient.

Table B.7
Dimensionless numbers for heat transfer, meaning and definition.

Symbol (name)	Definition	Meaning	Purpose
<i>Re</i> (REYNOLDS)	$\frac{\mathbf{v}L}{\nu}$	inertia- viscosity	Flow regime
<i>Pr</i> (PRANDTL)	$\frac{c_p \mu}{\lambda}$	momentum diffusion thermal diffusivity	Fluid characterization
<i>Nu</i> (NUSSELT)	$\frac{\alpha L}{\lambda}$	convective heat transfer conductive heat transfer	Heat transfer

[...] The fact that the interfaces are conceptualized as sharp interfaces means that they cannot store energy. Therefore, the amount of energy leaving one phase has to equal the amount of energy entering another phase. This has already been included in the equations, by the braces showing the individual energy fluxes \dot{e} .

[...] No Nu correlations for the case of multiphase flow in porous media could be found in the literature. Again, single-phase relations are employed [22].

$$\text{Nu} = 2 + 1.1\text{Pr}^{1/3}\text{Re}^{0.6} \quad (\text{B.2})$$

and a scaling factor f_e is assigned, allowing the study of the influence of the heat transfer. [...] Ultimately, f_e needs to be determined experimentally [17].

This is the very focus of this work: by calibrating the macro-scale model to experimental observations, we make a first step towards estimating heat transfer between phases in a two-phase flow in porous media setting.

Appendix C. Supplementary data

Supplementary data associated with this article can be found, in the online version, at <http://dx.doi.org/10.1016/j.ijheatmasstransfer.2015.04.057>.

References

- [1] 3M, August 2013. Products, 3m fluorinert electronic liquid fc-43. online. <<http://solutions.3m.com/wps/portal/3M/enUS/ElectronicsNA/Electronics/Products/ProductCatalog//3M-Fluorinert-Electronic-Liquid-FC-43?N=4294412766+5153906&Nr=AND%28hrcyid%3AXL6D5WDRG9gsC74XBTCBPBN2RL3FHVVKGPDK8BC31gv%29&rt=d>>.
- [2] B. Ahrenholz, J. Niessner, R. Helmig, M. Krafczyk, Pore-scale determination of parameters for macroscale modeling of evaporation processes in porous media, *Water Resour. Res.* (2011) 47.
- [3] A. Baytas, I. Pop, Free convection in a square porous cavity using a thermal nonequilibrium model, *Int. J. Therm. Sci.* 41 (9) (2002) 861–870. <<http://www.sciencedirect.com/science/article/pii/S1290072902013790>>.
- [4] F.L. Bookstein, Principal warps: thin-plate splines and the decomposition of deformations, *IEEE Trans. Pattern Anal. Mach. Intell.* 11 (6) (Jun 1989) 567–585.
- [5] S. Crone, C. Bergins, K. Strauss, Multiphase flow in homogeneous porous media with phase change, Part I: Numer. Model. *Transp. Porous Media* 49 (2002) 291–312. <<http://dx.doi.org/10.1023/A%3A1016271213503>>.
- [6] F. Fichot, F. Duval, N. Trégourès, N. Béchaud, M. Quintard, The impact of thermal non-equilibrium and large-scale 2D/3D effects on debris bed reflooding and coolability, *Nucl. Eng. Des.* 236 (19–21) (2006) 2144–2163. <<http://www.sciencedirect.com/science/article/pii/S0029549306002974>>.
- [7] P.A. Forsyth, Three-dimensional modelling of steam flush for DNAPL site remediation, *Int. J. Numer. Meth. Fluids* 19 (12) (1994) 1055–1081. <<http://dx.doi.org/10.1002/flid.1650191202>>.
- [8] Free Software Foundation, June 1991. GNU general public license, <<http://www.gnu.org/licenses/old-licenses/gpl-2.0.html>>.
- [9] R. Helmig, *Multiphase Flow and Transport Processes in the Subsurface: A Contribution to the Modeling of Hydrosystems*, Springer, 1997.
- [10] N.K. Karadimitriou, M. Musterd, P.J. Kleingeld, M.T. Kreutzer, S.M. Hassanizadeh, V. Joekar-Niasar, On the fabrication of PDMS micromodels by rapid prototyping, and their use in two-phase flow studies, *Water Resour. Res.* 49 (4) (2013) 2056–2067. <<http://dx.doi.org/10.1002/wrcr.20196>>.
- [11] N.K. Karadimitriou, P. Nuske, P.J. Kleingeld, S.M. Hassanizadeh, R. Helmig, Simultaneous thermal and optical imaging of two-phase flow in a micro-model, *Lab Chip* 14 (2014) 2515–2524. <<http://dx.doi.org/10.1039/C4LC00321G>>.
- [12] J. Mark, *Polymer Data Handbook*, Oxford University Press Incorporated, 1999. <<http://books.google.de/books?id=qFi5QgAACAAJ>>.
- [13] MATLAB, 2013. Matlab and image processing toolbox release 2013a. The MathWorks, Inc., Natick, Massachusetts, United States.
- [14] W. McAdams, *Heat Transmission*, McGraw-Hill, 1954. <<http://books.google.de/books?id=TWA-6yDCqCIC>>.
- [15] K. Mosthaf, K. Baber, B. Flemisch, R. Helmig, A. Leijnse, I. Rybak, B. Wohlmuth, A coupling concept for two-phase compositional porous-medium and single-phase compositional free flow, *Water Resour. Res.* (2011) 47.
- [16] Y. Mualem, A new model for predicting the hydraulic conductivity of unsaturated porous media, *Water Resour. Res.* 12 (3) (1976) 513–522. <<http://dx.doi.org/10.1029/WR012i003p00513>>.
- [17] P. Nuske, V. Joekar-Niasar, R. Helmig, Non-equilibrium in multiphase multicomponent flow in porous media: an evaporation example, *Int. J. Heat Mass Transfer* 74 (0) (2014) 128–142. <<http://www.sciencedirect.com/science/article/pii/S0017931014002178>>.
- [18] S.O. Ochs, H. Class, A. Färber, R. Helmig, Methods for predicting the spreading of steam below the water table during subsurface remediation, *Water Resour. Res.* 46 (5) (2010). <<http://dx.doi.org/10.1029/2007WR006401>>.
- [19] A. Oliveira, M. Kaviany, Nonequilibrium in the transport of heat and reactants in combustion in porous media, *Prog. Energy Combust. Sci.* 27 (5) (2001) 523–545. <<http://www.sciencedirect.com/science/article/pii/S0360128500000307>>.
- [20] U. Shavit, Special issue on transport phenomena at the interface between fluid and porous domains, *Transp. Porous Media* 78 (3) (2009) 327–330. <<http://dx.doi.org/10.1007/s11242-009-9414-1>>.
- [21] M. van Genuchten, A closed-form equation for predicting the hydraulic conductivity of unsaturated soils, *Soil Sci. Soc. Am. J.* 44 (5) (1980) 892–898.
- [22] N. Wakao, S. Kagei, *Heat and mass transfer in packed beds*, Topics in chemical engineering, Gordon and Breach Science Publishers, 1982. <<http://books.google.de/books?id=Ya5hzOgC05wC>>.